

# Solution Heat Treatment Optimization of Fourth-Generation Single-Crystal Nickel-Base Superalloys

HON TONG PANG, LIJUAN ZHANG, ROBBIE A. HOBBS, HOWARD J. STONE,  
and CATHERINE M.F. RAE

The optimization of the solution heat treatment (SHT) of fourth-generation single-crystal nickel-base superalloys LDSX-6B and LDSX-6C is presented. The methodological approach to optimizing the SHT process is particularly highlighted. Differential scanning calorimetry (DSC) measurements and electron-probe microanalysis (EPMA) mapping were carried out to investigate material properties in the as-cast condition and after SHT. The DSC equipment was also adopted as a vacuum furnace to evaluate the suitability of the SHT ramp profile and to check the safety margins with regard to incipient melting during SHT. SHT trials were carried out in a laboratory-scale vacuum furnace, after which the heat-treated samples were subjected to DSC experiments, microstructural analysis, and EPMA mapping to assess the effects of SHT peak temperatures and soak periods. From the DSC and EPMA results, as-cast LDSX-6B shows a lower degree of elemental microsegregation; hence, this alloy is relatively easier to homogenize in the SHT trials. In contrast, as-cast LDSX-6C was found to have a higher degree of elemental microsegregation; therefore, it is much more difficult to homogenize and is highly prone to incipient melting. The results of this study indicate that an increase in the SHT peak temperature and/or soak period will lead to an improved compositional homogeneity in the material as expected. After SHT, both alloys retained some residual elemental microsegregation and the LDSX-6C alloy showed precipitation of topologically close-packed (TCP) phase at the dendrite cores. The most appropriate and economic SHT process may be determined based on the methodological approach presented in this study and the requirements of the materials during service.

DOI: 10.1007/s11661-012-1146-0

© The Minerals, Metals & Materials Society and ASM International 2012

## I. INTRODUCTION

CURRENT economic and environmental pressures have increased the need for higher aeroengine efficiency to reduce the operating cost and environmental impact from increasing volumes of air travel. To achieve these targets, the engine operating temperature, specifically the turbine entry temperature (TET), has to be increased to improve the thermodynamic efficiency of the aeroengine. However, the current limitation on TET is the high-temperature capability of the materials used, as under such severe operating conditions, the materials in the hot section of the aeroengine, in particular the turbine blades and discs, must possess a good balance of high resistance to creep, fatigue, and environmental

deterioration under service conditions. Nickel-base superalloys have been the material of choice for hot sections of the aeroengine as this class of material offers a good balance of the required properties for operation in the severe high-temperature conditions. Nickel-base superalloys consist of a face-centered cubic (fcc)  $\gamma$  matrix phase and a coherent fcc  $\gamma'$  phase in the cuboidal precipitate morphology.

Turbine blades are cast as single crystals to confer higher creep resistance via the absence of grain boundaries. To achieve increasingly demanding creep strength requirements of turbine blades, increasing amounts of dense refractory elements are added to newer generations of single-crystal nickel-base superalloys for turbine blade applications.<sup>[1,2]</sup> Depending on the partitioning to either the  $\gamma$  or  $\gamma'$  phase, these dense refractory elements that include Mo, Re, Ta, W, and Ru may give solid-solution strengthening to the  $\gamma$  matrix phase, provide strengthening to the  $\gamma'$  precipitates phase, and/or increase the  $\gamma'$  precipitate volume fraction. In addition, these dense refractory elements have sluggish solute diffusivity; therefore, an improvement to creep properties may be expected.

The primary solidification of single-crystal nickel-base superalloy commences with the formation of  $\gamma$  dendrites. Solute partitioning at the solid-liquid interface occurs where the concentrations of elements that partition to  $\gamma$  (e.g., Re and W) are progressively reduced while the

---

HON TONG PANG, Research Associate, HOWARD J. STONE, Assistant Director of Research, and CATHERINE M.F. RAE, Reader, are with the Department of Materials Science and Metallurgy, University of Cambridge, Pembroke Street, Cambridge CB2 3QZ, U.K. Contact e-mail: htp21@cam.ac.uk LIJUAN ZHANG, formerly Research Associate, with the Department of Materials Science and Metallurgy, University of Cambridge, is now Senior Lecturer, with the School of Technology, University of Wolverhampton, Telford Campus, Telford TF2 9NT, U.K. ROBBIE A. HOBBS, formerly Project Manager, University Research (Materials) with Rolls-Royce plc., Derby DE24 8BJ, U.K., is now MBA Candidate, with the MIT Sloan School of Management, Cambridge, MA 02142.

Manuscript submitted October 18, 2010.

Article published online April 11, 2012

concentrations of elements that do not preferentially partition to  $\gamma$  (*i.e.*, partitions to  $\gamma'$ , *e.g.*, Al, Ti, and Ta) are enriched in the remaining liquid.<sup>[3]</sup> The slow solute diffusivity associated with the refractory content also means that significant elemental segregation arises during solidification. As a result, the as-cast microstructure of single-crystal turbine blades consists of severely cored  $\gamma$  dendrites and an interdendritic constituent with strong elemental segregation across the dendrites and interdendritic areas. Therefore, prior to service, the as-cast turbine blades need to be solution heat treated to homogenize the compositional segregation of the as-cast microstructure and to dissolve the  $\gamma'$  precipitates to allow these precipitates to be reprecipitated in the required morphology during subsequent aging heat treatments to confer the desired mechanical properties.

The highlighted solidification issues associated with the increased refractory content of newer generations of single-crystal superalloys also pose an increasing challenge to solution heat treatment (SHT). The significantly increased elemental segregation and slower solute diffusivity means that the material would require SHT at higher temperatures and longer times to achieve satisfactory compositional homogeneity.<sup>[4,5]</sup> This leads to increased costs of processing these alloys. Attempts to reduce the overall SHT duration by increasing the SHT peak temperature may cause incipient melting, *i.e.*, the occurrence of localized melting in the material, leading to material scrap. As such, careful considerations have to be given when devising the SHT cycles for these materials.

Previous approaches to designing the SHT cycles have mostly been based on trial and error. The SHT parameters of earlier generations of materials were very often adopted with modifications made to include additional steps during the SHT ramp and/or an alteration to the SHT peak temperature/soak period based on time-consuming and repeated furnace trials. This evolutionary approach lacks scientific rigor and may not be fully optimized to give the required compositional homogeneity in the materials at the optimum processing cost.

In this study, the optimization of the SHT of two fourth-generation single-crystal nickel-base superalloys LDSX-6B and LDSX-6C is presented, specifically highlighting the methodological approach to optimizing the SHT process. The approach assesses the thermal characteristics by using differential scanning calorimetry (DSC) measurements and the degree of elemental

microsegregation measured by employing electron-probe microanalysis (EPMA) to quantify the homogenization of the alloy. The novel element is that the same techniques are also used iteratively to evaluate separately the effects of both the ramp profile and the soak period of the SHT. For the purpose of clarity in the current study, the SHT cycle is divided into two parts, *i.e.*, (1) the ramp portion that follows a given SHT ramp profile prior to reaching the SHT peak temperature and (2) the soak portion that is the prolonged hold at SHT peak temperature to promote homogenization. The optimization process is as shown in Figure 1 and consists of the following steps:

- Evaluation of the thermal characteristics and the degree of elemental microsegregation of the as-cast material to provide a first estimate of the required SHT conditions
- Identification of suitable SHT ramp profile based on the thermal characteristics of the as-cast material
- Assessment of the suitability of the SHT ramp profile to reduce/eliminate elemental microsegregation between the dendrite and interdendritic areas (which has lower melting point) prior to reaching SHT peak temperature
- Assessment of the safety margins with regard to incipient melting during SHT in an industrial furnace for the chosen SHT ramp profile
- SHT trials in a laboratory-scale vacuum furnace to assess the compositional homogeneity attained as a function of SHT peak temperature and soak period

The different responses of the two alloys at various steps of the SHT optimization process are presented. At the end of the SHT optimization, the required SHT cycle could be determined based on the required compositional homogeneity of the material during service.

## II. MATERIALS

The materials used in this study were two fourth-generation single-crystal nickel-base superalloys LDSX-6B and LDSX-6C, with the nominal compositions as shown in Table I. These alloys were developed under the DARP SRR400 alloy development program.<sup>[6]</sup> The composition of LDSX-6B is specified for improvement in mechanical performance with its higher Ru content, whereas LDSX-6C is designed for improvement in

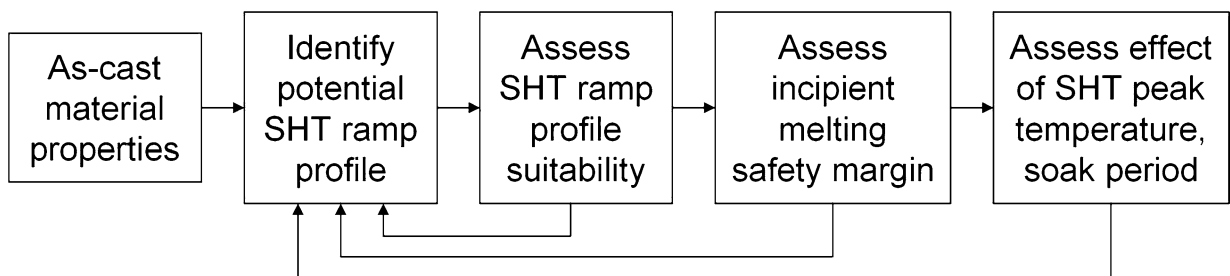


Fig. 1—Flow diagram detailing the solution heat treatment optimization process.

oxidation/environmental protection performance with its higher Cr content.

The materials for this study were received as test bars in the as-cast condition. The dimensions of the test bars were approximately 12 mm in diameter and 150 mm in length. The test bars were cast in a cluster assembly to produce 10 test bars per mold. Individual pigtail grain selector was used on each test bar during casting to favor growth of the  $\langle 001 \rangle$  along the longitudinal axes of the test bars. X-ray inspection was carried out on the test bars after casting, and the  $\langle 001 \rangle$  was within 10 deg from the longitudinal axes for all the test bars chosen for this study. The primary dendrite arm spacing of the test bars chosen were in the order of 200 to 250  $\mu\text{m}$ .

The microstructures of as-cast LDSX-6B and LDSX-6C were relatively similar as shown in Figure 2. These micrographs were obtained on a Camscan MX2600 field emission gun scanning electron microscope (Tescan USA, Inc., Cranberry Township, PA) operating at an accelerating voltage of 20 kV and a working distance of 10 mm in backscattered imaging mode. The samples were prepared according to standard metallographic preparation techniques, and at the final step, the samples were fine-polished with colloidal silica suspension. Dendrite lobes and interdendritic areas are clearly visible. The dendrite lobes were observed to have a distribution of  $\gamma$  and  $\gamma'$  phases. During primary solidification, the dendrites consist of the  $\gamma$  phase only; however, solid-state transformation of the  $\gamma$  phase to  $\gamma'$  precipitates occurs during cooling from solidification. The interdendritic pools were observed to have (1) fine  $\gamma/\gamma'$  morphology and (2) coarse cellular  $\gamma'$  structure separated by narrow  $\gamma$  channels.

### III. EXPERIMENTAL

#### A. As-Cast Material Properties

To obtain a first estimate of the required SHT parameters, the thermal characteristics of the materials in as-cast condition were quantified using DSC. A Netzsch DSC 404 (by Netzsch-Gerätebau GmbH, Selb, Germany) equipped with S-Type thermocouples (Pt10 pct Rh-Pt) in both the sample and the reference locations was used. The thermocouples were calibrated against the melting points of pure gold and pure nickel prior to the DSC measurements. The samples used for DSC measurements are approximately 5 mm in diameter and 1.5 mm in thickness, produced by electrodischarge machining (EDM). The samples were ground with SiC grinding paper to remove the EDM marks and finished to 2500-grit for the DSC experiment. Alumina crucibles were used in all DSC experiments. Prior to the start of measurement, the DSC was pumped down with a rotary/turbo vacuum pump combination to approximately  $5 \times 10^{-3}$  mbar and backfilled with argon; this procedure was repeated three times. Subsequent DSC measurement was carried out in a dynamic high-purity argon environment with an argon flow rate of 50 mL  $\text{min}^{-1}$ . During the DSC measurement, the temperature program used was heating at 20 K  $\text{min}^{-1}$  from room temperature to 873 K (600 °C) and thereafter at 10 K  $\text{min}^{-1}$  up to 1723 K (1450 °C), followed by a 15-minute dwell at 1723 K (1450 °C) and then cooling at 10 K  $\text{min}^{-1}$  from 1723 K to 1273 K (1450 °C to 1000 °C).

All the DSC traces and thermal data presented in this study are from the heating portion of the DSC experiments. The y-axes of the DSC traces presented are

**Table I. Nominal Compositions in Weight Percent of Fourth-Generation Single-Crystal Nickel-Base Superalloys LDSX-6B and LDSX-6C**

Element	Al	Ti	Cr	Co	Mo	Ru	Hf	Ta	W	Re	Ni
LDSX-6B	6.1	0.25	2.5	4	1	5	0.1	7	4.8	6.2	balanced
LDSX-6C	6.2	—	6.5	3	—	3	0.3	7	4.8	6.2	balanced

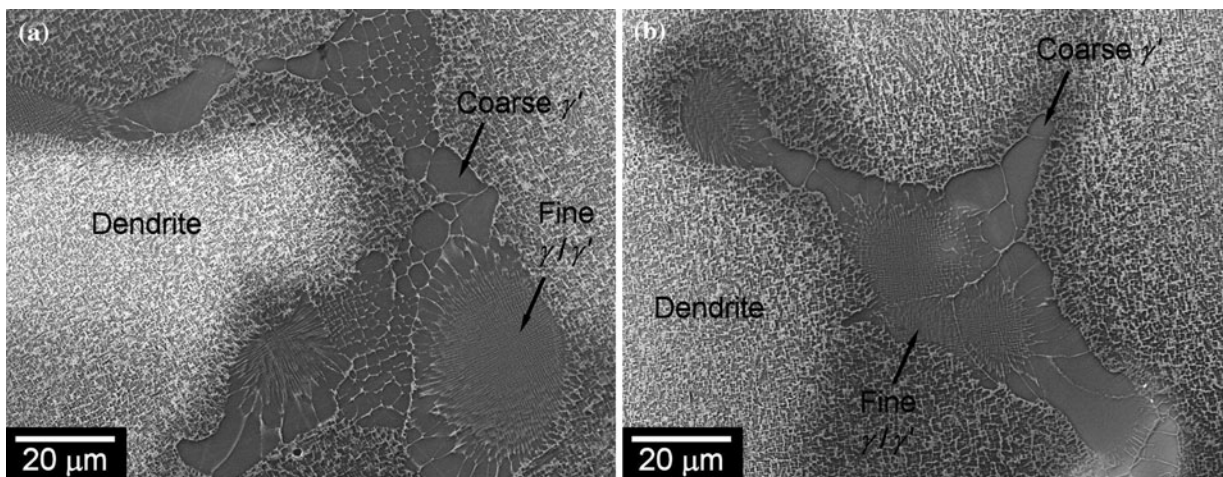


Fig. 2—Microstructures of test materials in as-cast condition: (a) LDSX-6B and (b) LDSX-6C.



aligned with the exothermic processes plotted in the positive  $y$ -direction. The thermal histories associated with the material and prior processing that determines the state of the material are captured in the data from the heating portion of the DSC experiment. The data from the cooling portion gives the phase transformation temperatures during cooling at  $10 \text{ K min}^{-1}$  and are therefore relatively similar for a particular alloy; this serves as a check of the alloy chemistry between samples of the same alloy and is usually found to be very consistent.

EPMA X-ray mapping of the alloys in as-cast condition was carried out to obtain a semiquantitative measure of the degree of elemental microsegregation in the as-cast materials. These results were to be compared with the results from solution heat-treated samples later. The samples used for EPMA X-ray mapping were prepared according to standard metallographic preparation techniques, and at the final step, the samples were fine-polished with colloidal silica suspension. A Cameca SX100 instrument was used to carry out EPMA X-ray mapping. The beam conditions were 20 kV and 100 nA, and the beam was fully focused (excitation volume for most X-rays in the alloy approximately 1 to 1.5 cubic microns). The map areas were  $750 \mu\text{m} \times 750 \mu\text{m}$ , and these areas were mapped at  $1 \mu\text{m}$  resolution with a dwell time of 40 ms at each location. The following X-ray lines were used (the choice of lines is constrained by the need to avoid significantly overlapping lines):

- (a)  $K\alpha_1$  Al, Ti, Cr, Co
- (b)  $L\alpha_1$  Mo, Ru, W, Re
- (c)  $M\alpha_1$  Hf, Ta

All calibration standards were pure (99.999 pct) metals except for Al, for which pure synthetic corundum ( $\text{Al}_2\text{O}_3$ ) was used. The analyzing crystals used were large lithium fluoride (LLiF) for Cr, Co, W, and Re; pentaerythritol (PET) for Ti, Mo, and Ru; large thallium acid phthalate (LTAP) for Hf and Ta; and thallium acid phthalate (TAP) for Al. Background positions and slope factors were determined using the Virtual WDS software (Cambridge Enterprise Ltd., Cambridge, U.K.).<sup>[7]</sup> The slope factors were calculated in place of measurements of background on the negative side of X-ray peaks for Mo and Ta, and on the positive side for W, Re, and Hf. Both backgrounds were measured for all other elements. Pulse height analysis with spectrometers in differential mode was used to eliminate interfering signals for Mo, Hf, and Ta.

### B. Identification of Potential SHT Ramp Profile

Based on the as-cast DSC results, two SHT ramp profiles with SHT peak temperatures of 1608 K and 1618 K (1335 °C and 1345 °C) as shown in Tables II and III were initially identified to be potentially suitable to be adopted for the two alloys; the 1608 K (1335 °C) ramp profile may be adopted for LDSX-6C whereas the 1618 K (1345 °C) ramp profile may be suitable for LDSX-6B. These ramp profiles have two intermediate dwell steps of 1-hour dwell and 3-hour dwell to promote homogenization prior to reaching the SHT peak temperature.

**Table II. 1608 K (1335 °C) SHT Ramp Profile**

$T$ Start [K (°C)]	$T$ End [K (°C)]	Ramp Time (min)	Soak Time at $T$ End (min)
293 (20)	1313 (1040)	120	15
1313 (1040)	1573 (1300)	60	20
1573 (1300)	1583 (1310)	40	60
1583 (1310)	1598 (1325)	60	180
1598 (1325)	1608 (1335)	60	soak

**Table III. 1618 K (1345 °C) SHT Ramp Profile**

$T$ Start [K (°C)]	$T$ End [K (°C)]	Ramp Time (min)	Soak Time at $T$ End (min)
293 (20)	1313 (1040)	120	15
1313 (1040)	1573 (1300)	60	20
1573 (1300)	1583 (1310)	40	60
1583 (1310)	1608 (1335)	60	180
1608 (1335)	1618 (1345)	60	soak

### C. SHT Ramp Profile Evaluation—Suitability Assessment

The DSC equipment was adopted as a mini vacuum furnace to assess the suitability of the SHT ramp profile as it represents the more reliable equipment in terms of temperature measurement and control. This is due to the proximity of the thermocouple to the sample; therefore, temperature measurement and control in the DSC equipment is expected to be more accurate compared to that of the full-size vacuum furnace. A “ramp run” was carried out in which a small sample of the as-cast material was subjected to the ramp profile in the DSC under vacuum, after which the sample was allowed to cool to room temperature, followed by a “measurement run” in the DSC to obtain the thermal characteristics of the ramped sample to evaluate the effects of the ramp profile. The 1618 K (1345 °C) ramp profile was simulated on LDSX-6B, whereas the 1608 K (1335 °C) ramp profile was simulated on LDSX-6C. These were followed by DSC measurements to quantify the thermal characteristics of these ramped samples.

### D. SHT Ramp Profile Evaluation—Incipient Melting Check

In this step, the safety margins with regard to incipient melting during SHT in an industrial environment were assessed for the chosen SHT ramp profiles. This step is necessary to take into account the temperature spread that may be expected in a large industrial furnace. The DSC equipment was again adopted as a mini vacuum furnace for this step due to its ability to give better accuracy in temperature measurements. As before, a “ramp run” was carried out by subjecting a small sample of the as-cast material to the ramp profile in vacuum. However, the end temperature was altered, either by increasing the end temperature above the SHT peak temperature (at similar heating rate to the final

step) to check the safety margins or by halting at temperatures below the intended SHT peak temperature to check for the onset of incipient melting. The “ramp run” was halted when the desired temperature was achieved, and the sample was allowed to cool to room temperature and subsequently metallographically prepared to check for evidence of incipient melting using an optical microscope.

The as-cast LDSX-6B alloy was subjected to the 1618 K (1345 °C) ramp profile but with the end temperature extended to 1623 K (1350 °C); note that the maximum temperature recorded by the DSC for this ramp run was only 1621 K (1348 °C). For the as-cast LDSX-6C material, initial DSC runs to check for incipient melting were carried out using the 1608 K (1335 °C) ramp profile, with the end temperature set to hit 1603 K and 1608 K (1330 °C and 1335 °C). The actual temperatures achieved in these runs were 1599 K and 1606 K (1326 °C and 1333 °C), respectively.

A new ramp profile with a SHT peak temperature of 1593 K (1320 °C) (Table IV) has to be devised for LDSX-6C as the 1608 K (1335 °C) ramp profile was found to be unsuitable for LDSX-6C. The 1593 K (1320 °C) ramp profile is based on the 1608 K (1335 °C) ramp profile but with the temperatures adjusted accordingly at each step to give a SHT peak temperature of 1593 K (1320 °C); the rationale behind the chosen temperatures will be provided in Section V. Incipient melting check using the 1593 K (1320 °C) ramp profile was carried out with the end temperatures set to hit 1593 K, 1598 K, and 1603 K (1320 °C, 1325 °C, and 1330 °C) (at a similar heating rate to the final step). The actual maximum temperatures achieved during these DSC ramp runs were 1592 K, 1597 K, and 1602 K (1319 °C, 1324 °C, and 1329 °C), respectively.

#### E. SHT Peak Temperature and Soak Period Evaluation

The effects of the SHT peak temperature and soak period on the attained compositional homogeneity were assessed in this section. The SHT runs were carried out in an AFT vacuum furnace (by Advanced Furnace Technology, Cambridge, U.K.). The furnace uses a graphite heating element, and temperature control was achieved with a C-type thermocouple (W26 pct Rh-W5 pct Rh) located near the heating element. The hot zone size was approximately 100 mm in diameter and 100 mm in height. The temperature in the center of the hot zone was calibrated against the melting points of pure gold and pure nickel prior to the SHT runs, and

during the SHT runs, the alloy samples were placed at this location. Within the hot zone, the temperature uniformity was within  $\pm 1$  °C as determined by scanning the hot zone with a separate R-type thermocouple during the calibration process. The alloy samples used for the SHT runs are approximately 12 mm in diameter and 10 mm thick. After the SHT runs in the vacuum furnace, samples were prepared for DSC measurements, microstructural examination, and EPMA X-ray mappings.

For LDSX-6B, the effects of soak period on homogeneity following the 1618 K (1345 °C) ramp were assessed with two soak periods of 20 and 40 hours. For reasons that will become apparent in Section IV, an additional SHT run was also carried out at 1633 K (1360 °C) with a 20-hour soak period to assess the effects of SHT peak temperatures, *i.e.*, 1618 K (1345 °C) vs 1633 K (1360 °C) at a given soak period of 20 hours. The 1633 K (1360 °C) ramp profile as shown in Table V is based on the 1618 K (1345 °C) ramp profile, with some of the critical temperatures raised accordingly to promote the homogenization process.

For the solutioning of LDSX-6C, the effects of soak period on homogeneity following the 1593 K (1320 °C) ramp were assessed with three soak periods of 20, 40, and 80 hours. Another trial was carried out using the 1588 K (1315 °C) ramp (Table VI) with a soak period of 40 hours to allow for a comparison with the results of the 1593 K (1320 °C)/40 hours SHT cycle. All the critical temperatures of the 1588 K (1315 °C) ramp were adjusted to be 5 °C lower compared to the 1593 K (1320 °C) ramp. These lower temperatures are expected to mimic the temperatures experienced in the cold spots of an industrial vacuum furnace for the 1593 K (1320 °C) ramp; hence, it would be of interest to assess the response of LDSX-6C to the 1588 K (1315 °C)/40 hours SHT cycle.

**Table IV. 1593 K (1320 °C) SHT Ramp Profile**

<i>T</i> Start [K (°C)]	<i>T</i> End [K (°C)]	Ramp Time (min)	Soak Time at <i>T</i> End (min)
293 (20)	1313 (1040)	120	15
1313 (1040)	1573 (1300)	60	20
1573 (1300)	1583 (1310)	40	60
1583 (1310)	1588 (1315)	60	180
1588 (1315)	1593 (1320)	60	soak

**Table V. 1633 K (1360 °C) SHT Ramp Profile**

<i>T</i> Start [K (°C)]	<i>T</i> End [K (°C)]	Ramp Time (min)	Soak Time at <i>T</i> End (min)
293 (20)	1313 (1040)	120	15
1313 (1040)	1593 (1320)	60	20
1593 (1320)	1603 (1330)	40	60
1603 (1330)	1623 (1350)	60	180
1623 (1350)	1633 (1360)	60	soak

**Table VI. 1588 K (1315 °C) SHT Ramp Profile**

<i>T</i> Start [K (°C)]	<i>T</i> End [K (°C)]	Ramp Time (min)	Soak Time at <i>T</i> End (min)
293 (20)	1313 (1040)	120	15
1313 (1040)	1563 (1290)	60	20
1563 (1290)	1573 (1300)	40	60
1573 (1300)	1583 (1310)	60	180
1583 (1310)	1588 (1315)	60	soak

## IV. RESULTS

### A. As-Cast Material Properties

The DSC results of the materials in as-cast condition are shown in Figure 3. Two measurement runs were carried out for each alloy. In general, as the temperature is increased, the initially horizontal bulk solid line starts to show a gentle exothermic deviation with an approximately constant slope, which is associated with the solid-state dissolution of the  $\gamma'$  precipitates. This is followed by two endothermic peaks; a first smaller peak at a particular temperature followed by a larger peak at a slightly higher temperature. The first small endothermic peak indicates the melting of the interdendritic region; from here forward, the first small peak will be referred to as the interdendritic peak. The larger peak that follows the interdendritic peak indicates the melting of the bulk of the alloy, *i.e.*, the  $\gamma$  dendrites in the material; hereafter, the larger peak will be referred to as the bulk melting peak.

The approximate temperatures at which the phase transformations occur, *i.e.*, the  $\gamma'$  solvus start,  $\gamma'$  solvus end, incipient melting temperature ( $T_{IM}$ ), and bulk melting temperature ( $T_{BM}$ ) were identified by examining the first and second derivatives (with respect to time) of the DSC traces. At a constant heating rate, the time-derivative  $d(\text{DSC})/dt$  is proportional to the temperature-derivative  $d(\text{DSC})/dT$ . The  $\gamma'$  solvus start and  $\gamma'$  solvus end were determined by inspecting the first derivative trace for changes in the gradient of the associated gentle exothermic deviation on the DSC trace. The  $T_{IM}$  and  $T_{BM}$  were determined from the corresponding peaks on the DSC curves, at the point where endothermic deviation is first detected (first derivative crosses below 0), or at the inflection point (second derivative = 0). The  $T_{IM}$  is the temperature at which localized melting in the interdendritic regions starts to occur, and it is taken as the temperature at which the DSC trace (heating portion) first exhibits an endothermic deviation from the tangent of the bulk solid line near the onset of the interdendritic peak. However, if the degree of incipient melting is extremely small, *e.g.*, <1 pct volume, then the

DSC is unlikely to have the sensitivity to detect the occurrence of incipient melting. The  $T_{BM}$  is the temperature where bulk melting of the alloy commences, and this temperature is inferred from the onset of the bulk melting peak. Note that the  $T_{BM}$  obtained from these methods are only an approximation of the actual bulk melting temperature. The raw DSC signal is assumed to be proportional to the specific heat capacity difference between the sample and the reference, which has been pointed out by Boettinger and Kattner<sup>[8]</sup> to be *only true* when no latent heat evolves in the sample during melting and solidification. However, the latent heat always evolves in the sample during melting and solidification, as such, the raw DSC signal is smeared over a range of temperatures; hence, approximating the  $T_{BM}$  from the heating portion of the raw DSC trace (after which some local incipient melting has occurred above  $T_{IM}$ ) is, strictly speaking, not exact. Nevertheless, *within* the context of this study, the  $T_{BM}$  obtained from the raw DSC signal should enable comparisons of the phase transition temperatures to be made after the alloys were subjected to the various SHT ramps and soak periods. Care should be exercised when comparing the  $T_{BM}$  obtained from the raw DSC signal in this study to the  $T_{BM}$  obtained from DSC curves that have been corrected against latent heat evolution during melting in other studies.<sup>[9]</sup>

For both alloys in the as-cast condition, the solid-state dissolution of the  $\gamma'$  precipitates occurs over a range of temperatures rather than at a distinct temperature, as indicated by the gentle exothermic reaction over a range of temperatures after the  $\gamma'$  solvus start temperature. The end of the  $\gamma'$  dissolution, *i.e.*, the end of the exothermic deviation, seems to commensurate with  $T_{IM}$ , which is the start of the interdendritic peak. The shape and magnitude of the interdendritic and bulk melting peaks are significantly different between the two alloys. For as-cast LDSX-6B, the interdendritic peak is relatively minor but is very close and immediately followed by the bulk melting peak, to the point where they overlap and there is no distinct trough separating these two peaks. An inflection point on the DSC trace to

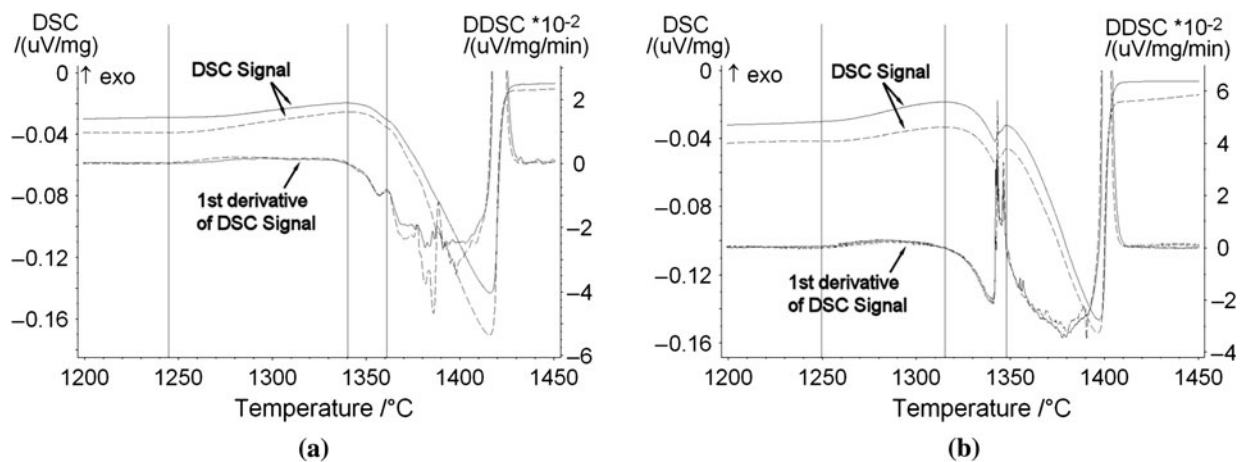


Fig. 3—DSC results of as-cast material: (a) LDSX-6B and (b) LDSX-6C.



separate these two peaks could be inferred when inspecting the first derivative of the DSC signal; the temperature at the inflection point was taken to be  $T_{BM}$  for LDSX-6B. For as-cast LDSX-6C, the interdendritic peak and bulk melting peak were separate and distinct, and the proportion of the interdendritic peak relative to the bulk melting peak was noted to be much larger compared to corresponding peaks of as-cast LDSX-6B. In Figure 3, the vertical lines indicate the  $\gamma'$  solvus start temperature,  $T_{IM}$ , and  $T_{BM}$  as obtained by examining the first and second derivatives of the DSC signal, and the values are shown in Table VII.

EPMA maps to show the degree of elemental microsegregation in the as-cast materials are shown in Figure 4. Note that the same scaling was used for the maps of a given element to enable a comparison of the two alloys. The maps show the typical behavior for single-crystal superalloys in the as-cast condition, where Cr, Co, Mo, Ru, W, and Re are concentrated in the dendrite cores and dendrites due to preferential partitioning of these elements to the solid during solidification, whereas Al, Ti, Hf, and Ta are concentrated in the interdendritic regions due to preferential partitioning to the liquid during solidification. Severe partitioning of W and Re in the dendrite cores were observed from the maps, while strong partitioning of Al and Ta were particularly distinct in the interdendritic regions. Al, W, and Re are therefore good indicators of the compositional homogeneity. Another distinct observation is the concentration of Cr which seems to be generally weaker in the interdendritic regions compared to the dendritic areas, but there is a much higher concentration of Cr at one edge of any given interdendritic pool even beyond the concentration of Cr in the dendritic areas. The enrichment of Cr in these areas also seems to coincide with higher concentrations of Hf in these areas.

EPMA maps of the as-cast materials indicate a higher degree of elemental microsegregation in LDSX-6C. Both alloys have similar contents of Al, Ta, and Re (Table I); however, the EPMA maps of these elements indicate a slightly higher degree of elemental microsegregation of these elements in LDSX-6C. Segregation of the elements Cr and Hf in LDSX-6C were more distinct as this alloy has much higher content of these elements compared to LDSX-6B. Another point to note is that in LDSX-6C, Ti was not specified in the alloy composition but was found in the alloy during EPMA analysis. This was due to Ti contamination in LDSX-6C introduced during the production process by the use of CMSX-4 melt pennies.

**Table VII. Thermal Characteristics of LDSX-6B and LDSX-6C in As-Cast Condition**

	$\gamma'$ Solvus Start [K (°C)]	$T_{IM}$ [K (°C)]	$T_{BM}$ [K (°C)]
As-cast LDSX-6B	1518 (1245)	1613 (1340)	1634 (1361)
As-cast LDSX-6C	1523 (1250)	1588 (1315)	1621 (1348)

## B. DSC Runs for SHT Ramp Profile Evaluation

The DSC trace of as-cast LDSX-6B that has been subjected to the 1618 K (1345 °C) ramp is shown in Figure 5(a). The interdendritic peak observed in the as-cast condition was completely eliminated, and  $T_{BM}$  was shifted to a slightly higher temperature of 1637 K (1364 °C) compared to  $T_{BM}$  of 1634 K (1361 °C) in the as-cast condition. Due to the lack of the interdendritic peak, the start of melting occurs at 1637 K (1364 °C) with localized melting of the bulk material after the 1618 K (1345 °C) ramp compared to the as-cast condition where melting starts at 1613 K (1340 °C) with localized incipient melting in the interdendritic areas.

Figure 5(b) shows the DSC trace for as-cast LDSX-6C that has been subjected to the 1608 K (1335 °C) ramp. At first glance, the interdendritic peak seems to be removed, but on closer inspection, a very slight peak could still be detected as shown in Figure 6. The  $T_{IM}$  of LDSX-6C was approximately 1601 K (1328 °C) after the 1608 K (1335 °C) ramp compared to the as-cast  $T_{IM}$  of 1588 K (1315 °C). The  $T_{IM}$  after ramp was therefore lower compared to the peak temperature of the 1608 K (1335 °C) ramp. Incipient melting would have occurred in the material during the ramp, which was shown to be the case in the next section detailing DSC runs to check incipient melting. Therefore, strictly speaking, the interdendritic peak and  $T_{IM}$  are associated with the interdendritic regions that have been melted as the temperature is increased above the local  $T_{IM}$  during the ramp and resolidified on cooling after the ramp. The 1608 K (1335 °C) ramp was therefore unsuitable for SHT of LDSX-6C, as the ramp was unable to reduce the elemental microsegregation sufficiently to prevent incipient melting in this material prior to reaching the intended SHT peak temperature.

For both alloys, the  $\gamma'$  solvus in each alloy becomes much more abrupt after the material was subjected to the ramp. The vertical lines in Figures 5 and 6 indicate the  $\gamma'$  solvus start temperature,  $\gamma'$  solvus end temperature,  $T_{IM}$ , and  $T_{BM}$ , the values as summarized in Table VIII.

## C. DSC Runs for Incipient Melting Check

The microstructure of LDSX-6B that has been subjected to the 1618 K (1345 °C) ramp but with the end temperature extended to 1621 K (1348 °C) is shown in Figure 7. Incipient melting was not observed in the microstructure. A minimal amount of remnant interdendritic areas from casting was observed (indicated by arrows), which agrees relatively well with the DSC results in Figure 5(a) showing the absence of the interdendritic peak after the material was subjected to the 1618 K (1345 °C) ramp. The absence of the interdendritic peak would suggest that the interdendritic areas have been completely dissolved; however, the minimal interdendritic areas still observed in the microstructure reiterate the limits of the DSC in detecting very small volumes of phase transformation, in this case the melting of the minimal amount of remnant interdendritic areas.

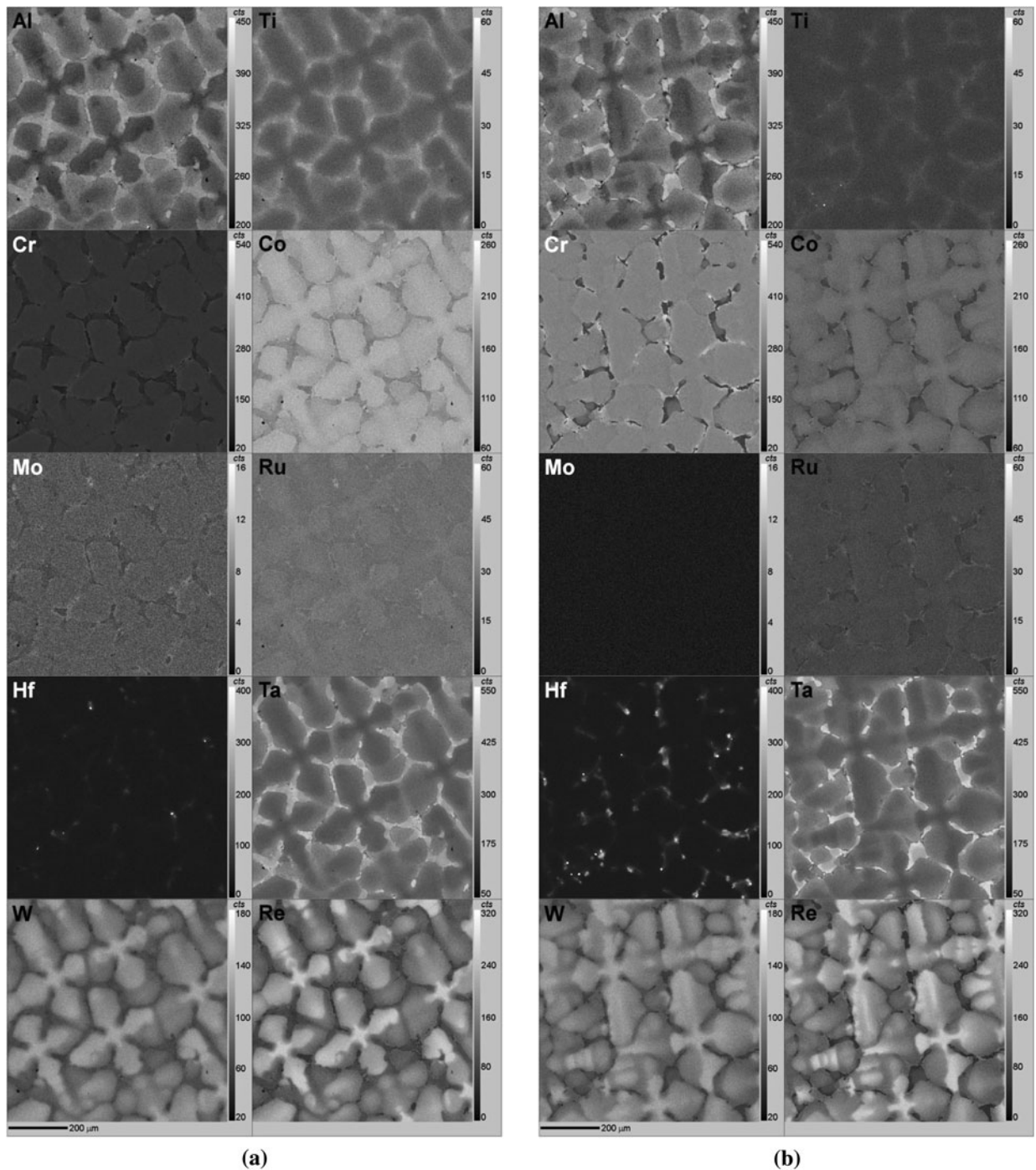


Fig. 4—EPMA maps of test materials in as-cast condition: (a) LDSX-6B and (b) LDSX-6C.

The microstructures of LDSX-6C that have been subjected to the 1608 K (1335 °C) ramp but halted at two temperatures at 1599 K and 1606 K (1326 °C and 1333 °C), are shown in Figure 8. The “flower-like” or “bulls-eye” features at pores observed in both samples are clear signs of incipient melting. The  $T_{IM}$  of 1601 K (1328 °C) as shown in Table VIII after the 1608 K (1335 °C) ramp is therefore associated with the lowest melting point areas in these melted interdendritic areas. Another point to note is that incipient melting was

observed in the LDSX-6C sample that has experienced a maximum temperature of 1599 K (1326 °C) even though the  $T_{IM}$  was found to be 1601 K (1328 °C) after the 1608 K (1335 °C) ramp. This finding is again likely to be related to the limits of the DSC in detecting small degree of incipient melting, in this case between 1599 K and 1601 K (1326 °C and 1328 °C).

In light of the results from the SHT ramp profile evaluation and the incipient melting check, which highlighted the unsuitability of the 1608 K (1335 °C)



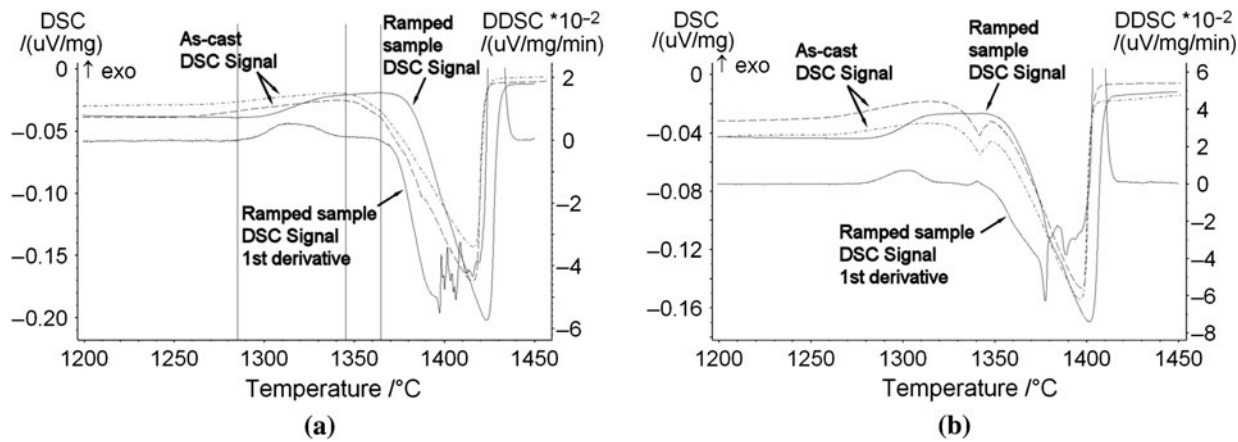


Fig. 5—DSC results after ramp: (a) LDSX-6B after 1618 K (1345 °C) ramp and (b) LDSX-6C after 1608 K (1335 °C) ramp.

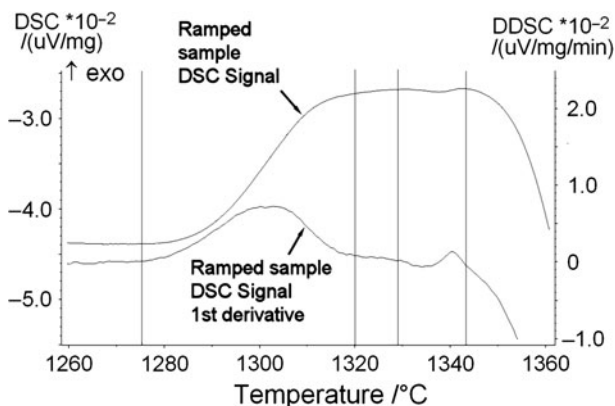


Fig. 6—DSC results of LDSX-6C after 1608 K (1335 °C) ramp in greater detail.

ramp for LDSX-6C, additional incipient melting check was carried out with the newly devised 1593 K (1320 °C) ramp profile (Table IV). The microstructures of LDSX-6C after the 1593 K (1320 °C) ramp and with the maximum temperatures modified to achieve 1592 K, 1597 K, and 1602 K (1319 °C, 1324 °C and 1329 °C) are shown in Figure 9. For the sample subjected to a maximum temperature of 1592 K (1319 °C), remnant interdendritic areas from the casting process with irregular shapes was readily observed in the sample, but incipient melting was not seen. After the sample was subjected to a maximum temperature of 1597 K (1324 °C), remnant interdendritic area from the casting process was again observed, although the amount was reduced compared to the 1592 K (1319 °C) sample. On closer inspection, the 1597 K (1324 °C) sample showed some minor incipient melting at the smaller pores as shown in Figure 9(d). For the sample subjected to the highest maximum temperature of 1602 K (1329 °C), an even lower amount of remnant interdendritic areas was observed, but the occurrence of incipient melting at small pores was very much increased as shown in Figures 9(e) and (f). In this series of incipient melting check experiments, the maximum temperatures of 1592 K, 1597 K, and 1602 K (1319 °C, 1324 °C, and 1329 °C) were

achieved at the same heating rate to that of the final step; therefore, in addition to being an incipient melting check, this particular series of experiments also serve as a down-selection route for the SHT peak temperature that may be used. Since minor incipient melting has been observed in the 1597 K (1324 °C) sample, the SHT peak temperature for LDSX-6C was appropriately limited to 1593 K (1320 °C), as per the devised 1593 K (1320 °C) ramp profile in Table IV, which should reduce the risk of significant localized incipient melting after taking into account the temperature variability that may be expected within an industrial furnace.

#### D. SHT Peak Temperature and Soak Period Evaluation

To study the effects of SHT peak temperature and soak period, the LDSX-6B alloy was subjected to three SHT trials, which were 1618 K (1345 °C)/20 hours, 1618 K (1345 °C)/40 hours, and 1633 K (1360 °C)/20 hours, where the time denotes the soak period at SHT peak temperature. To highlight the potential effects of the SHT peak temperature, the SHT peak temperature of 1633 K (1360 °C) was chosen in light of the ramp profile evaluation results, where after the 1618 K (1345 °C) ramp, the interdendritic peak was removed and the  $T_{BM}$  was raised to 1637 K (1364 °C). Therefore, the SHT peak temperature could be as high as 1633 K (1360 °C) if the temperature fluctuations in the furnace could be controlled to within  $\pm 3$  °C. Neither remnant interdendritic nor incipient melting was observed in the LDSX-6B samples after the three SHT trials. The DSC results of LDSX-6B after the SHT trials are shown in Figure 10, and all three DSC traces show a flat plateau prior to the bulk melting peak, indicating the absence of remnant interdendritic areas in agreement with the observed microstructure. The thermal characteristics of LDSX-6B after the SHT trials are summarized in Table IX.

The compositional homogeneity of LDSX-6B after the SHT trials is shown by EPMA maps of Al, W, and Re (which are more strongly segregating) in Figure 11. Remnant interdendritic areas were not observed in agreement with the DSC traces. Comparing the effects

**Table VIII. Thermal Characteristics of LDSX-6B and LDSX-6C After SHT Ramp**

	$\gamma'$ Solvus Start [K (°C)]	$\gamma'$ Solvus End [K (°C)]	$T_{IM}$ [K (°C)]	$T_{BM}$ [K (°C)]
LDSX-6B 1618 K (1345 °C) Ramp	1558 (1285)	1618 (1345)	—	1637 (1364)
LDSX-6C 1608 K (1335 °C) Ramp	1548 (1275)	1593 (1320)	1601 (1328)	1616 (1343)

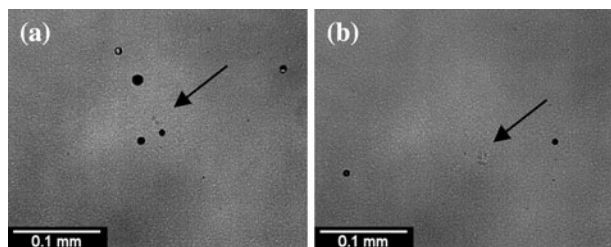


Fig. 7—Microstructure of LDSX-6B after 1618 K (1345 °C) ramp in DSC, maximum temperature ~1621 K (1348 °C).

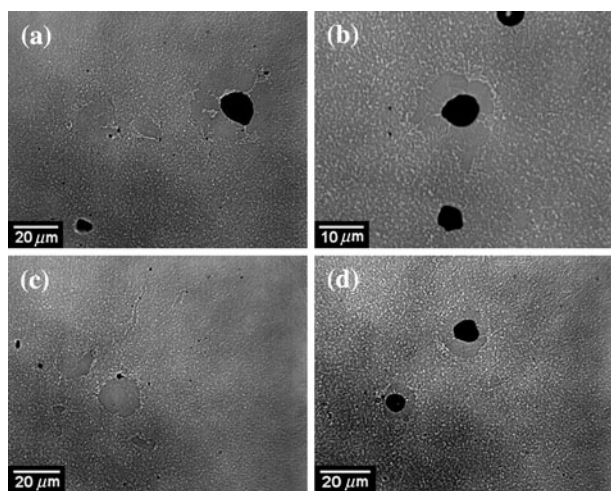


Fig. 8—Microstructures of LDSX-6C after 1608 K (1335 °C) ramp in DSC: (a and b) maximum temperature ~1599 K (1326 °C) and (c and d) maximum temperature ~1606 K (1333 °C).

of the soak period at 1618 K (1345 °C) on the homogeneity of LDSX-6B, greater segregation of Al, W, and Re was observed after the 20 hours soak compared to the 40 hours soak. At a constant soak period of 20 hours, an increase in the SHT peak temperature from 1618 K to 1633 K (1345 °C to 1360 °C) resulted in a much lower segregation of Al, W, and Re (Figures 11(a) and (c)). However, a comparison of Figures 11(a) through (c) shows that doubling the soak period from 20 hours to 40 hours at 1618 K (1345 °C) is more effective in reducing the elemental segregation than an increase of 15 °C in the SHT peak temperature from 1618 K to 1633 K (1345 °C to 1360 °C) at a constant soak period of 20 hours.

The LDSX-6C alloy was subjected to four SHT trials which were 1588 K (1315 °C)/40 hours, 1593 K (1320 °C)/20 hours, 1593 K (1320 °C)/40 hours, and

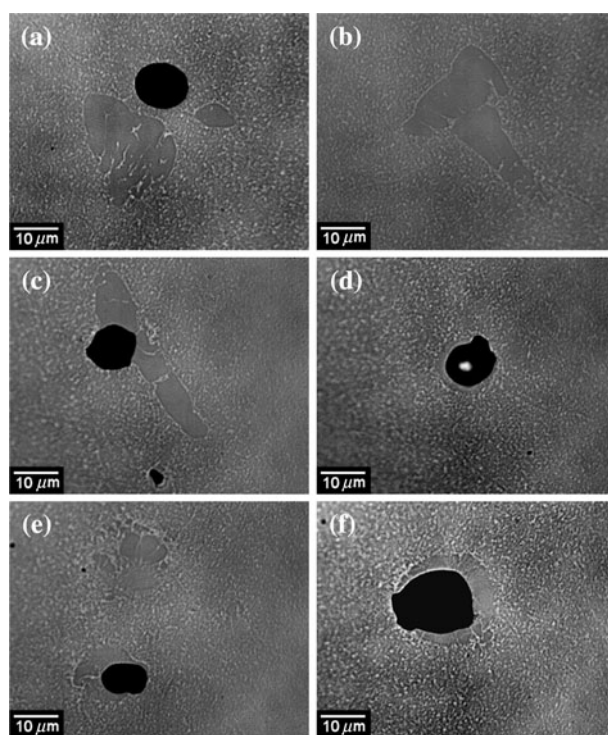


Fig. 9—Microstructure of LDSX-6C after 1593 K (1320 °C) ramp in DSC: (a and b) maximum temperature ~1592 K (1319 °C), (c and d) maximum temperature ~1597 K (1324 °C), and (e and f) maximum temperature ~1602 K (1329 °C).

1593 K (1320 °C)/80 hours to study the effects of SHT peak temperature and soak period. The microstructure after SHT at 1588 K (1315 °C)/40 hours (Figure 12(a)) indicates the presence of a significant amount of remnant interdendritic areas from the casting process. A much lower amount of remnant interdendritic areas was observed after SHT at 1593 K (1320 °C)/20 hours. After SHT at 1593 K (1320 °C)/40 hours and 1593 K (1320 °C)/80 hours, remnant interdendritic areas were no longer observed. The microstructure of LDSX-6C after the SHT trials frequently shows the presence of fine needle-like precipitates as shown in Figure 12(b), which were mostly restricted to dendrite cores. These precipitates were identified as topologically close-packed (TCP) phases by EPMA maps, which showed high concentrations of W and Re in these precipitates (Figure 13).

The DSC results of LDSX-6C after the SHT trials are shown in Figure 14. After SHT at 1588 K (1315 °C)/40 hours, a minor interdendritic peak could still be observed at the end of the flat plateau before the onset of the bulk melting peak. This finding corresponds with the remnant interdendritic areas observed Figure 12(a).

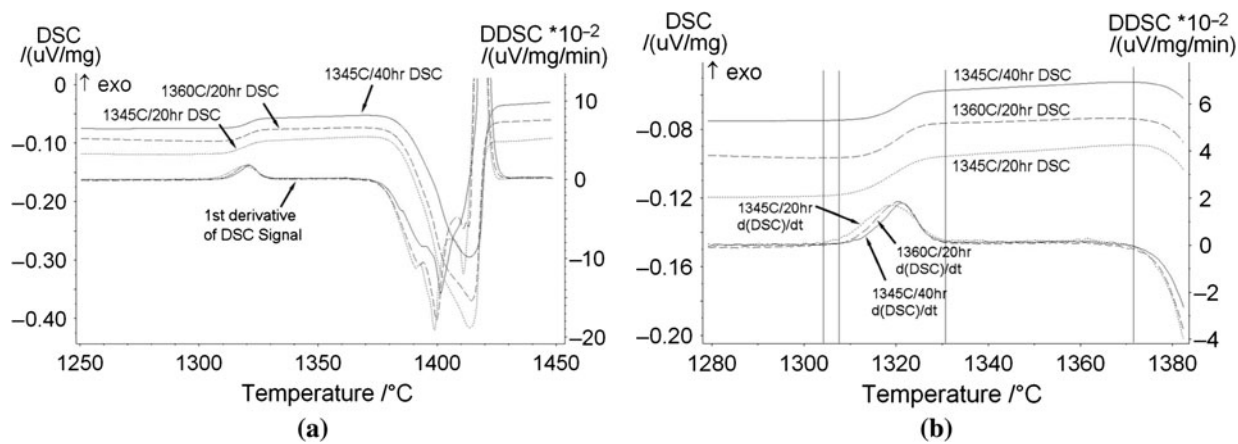


Fig. 10—DSC results of LDSX-6B after SHT trials (a), and (b) in higher detail.

Table IX. Thermal Characteristics of LDSX-6B After SHT Trials

	$\gamma'$ Solvus Start [K (°C)]	$\gamma'$ Solvus End [K (°C)]	$T_{IM}$ [K (°C)]	$T_{BM}$ [K (°C)]
1618 K (1345 °C)/20 h	1577 (1304)	1604 (1331)	—	1644 (1371)
1618 K (1345 °C)/40 h	1581 (1308)	1605 (1332)	—	1644 (1371)
1633 K (1360 °C)/20 h	1581 (1308)	1604 (1331)	—	1644 (1371)

After SHT at 1593 K (1320 °C)/20 hours, an extremely gentle minor interdendritic peak was still observed, again corresponding to the relatively small remnant interdendritic areas observed in the microstructure. After SHT at 1593 K (1320 °C)/40 hours and 1593 K (1320 °C)/80 hours, a flat plateau was observed followed by the onset of bulk melting without any discernable interdendritic peak, although a very slight inflection was noted on the first derivative curve even though remnant interdendritic areas were not observed in both samples. From these DSC traces, the exothermic reaction associated with the solid-state dissolution of the  $\gamma'$  precipitates was also noted to become progressively more abrupt with longer soak time at 1593 K (1320 °C). The thermal characteristics of LDSX-6C after the SHT trials are summarized in Table X.

EPMA maps of Al, W, and Re for LDSX-6C solutioned at 1593 K (1320 °C) for 20 hours, 40 hours, and 80 hours are shown in Figure 13. A progressive reduction in the elemental micro-segregation of Al, W, and Re with longer soak periods at 1593 K (1320 °C) was observed, indicating a progressive improvement in the compositional homogeneity with longer soak periods as expected. Note the needle-like TCP phases rich in W and Re in the dendrite cores.

## V. DISCUSSION

### A. Optimization of SHT Cycle

The principal purpose of SHT is to dissolve the irregular-shaped  $\gamma'$  precipitates that arise from the casting process to be renucleated as fine precipitates during cooling from SHT and aged to achieve the

desired precipitate size and a refined regular morphology during the aging heat treatments to confer the required mechanical properties. With the increasing refractory contents of newer generations of single-crystal nickel-base superalloys, the SHT process also serves to homogenize the material with regard to reducing the elemental segregation that arises due to preferential elemental partitioning of the heavy refractory elements to solid or liquid during the solidification process. The latter, which has had less emphasis in conventional foundry practice, is essential to minimize instability with respect to TCP phases and to make the best use of these expensive and dense additions. To satisfy these two requirements, the SHT temperature has to be above the  $\gamma'$  solvus temperature, strictly speaking, the  $\gamma'$  solvus end temperature, to dissolve all the  $\gamma'$  precipitates, and below the melting point ( $T_{IM}$  or  $T_{BM}$ ) of the alloy. The temperature range between these lower and upper bounds is known as the SHT window.

The temperatures used in the ramp are effectively bound by local incipient melting, usually in the interdendritic regions of the microstructure, and the role of the ramp is to increase the  $T_{IM}$  as rapidly as possible within the constraints of the furnace used. During the ramp, progressive reduction of elemental segregation between the dendrite and interdendritic areas occurs by diffusion; this is accompanied by dissolution of the interdendritic areas and an increase in the  $T_{IM}$ . In addition, the  $\gamma'$  solvus temperatures were also noted to become more distinct during ramp. Therefore, the SHT window is dynamic as both the  $\gamma'$  solvus end temperature progressively shifts to lower temperatures (approaching  $\gamma'$  solvus end temperature of the fully homogenized condition) and the  $T_{IM}$  associated with the interdendritic areas progressively



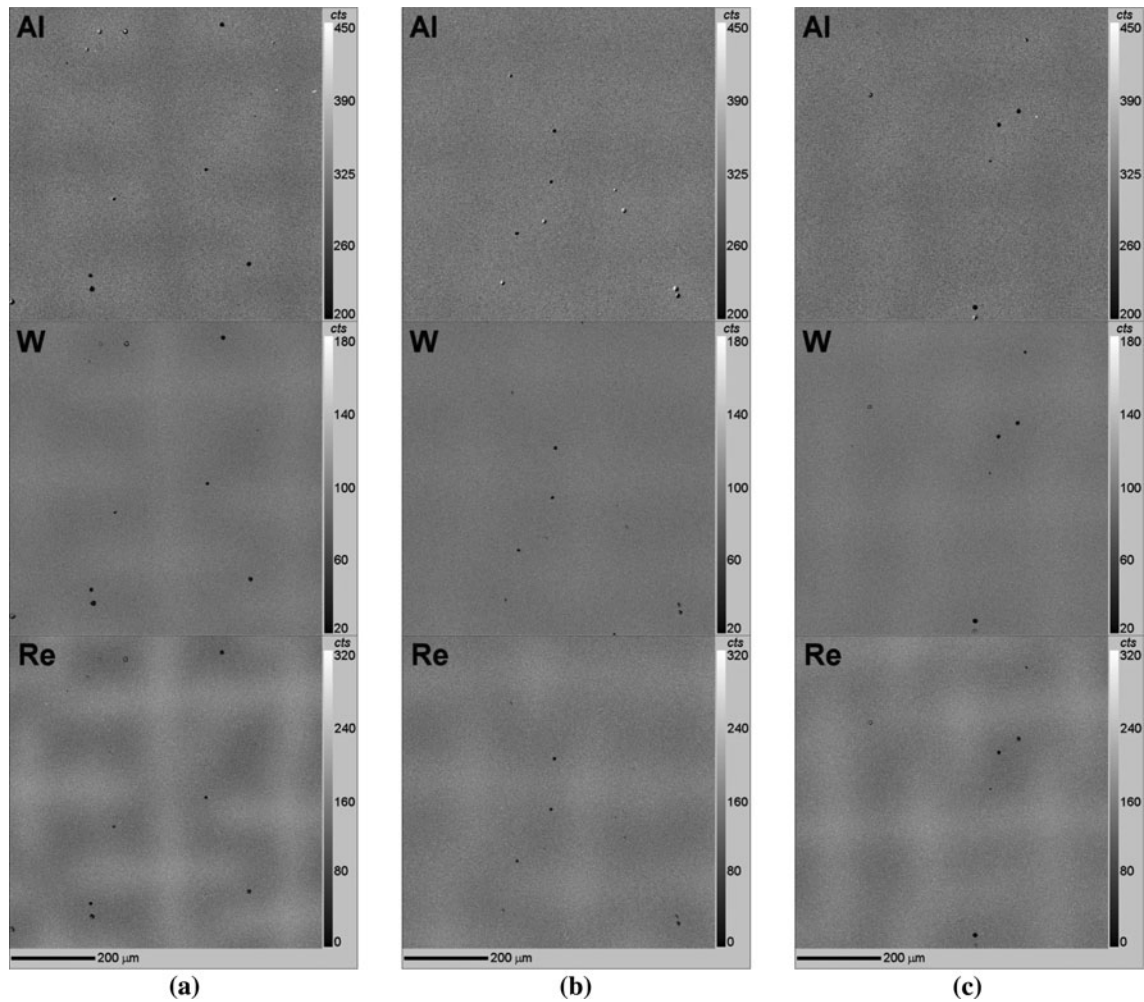


Fig. 11—EPMA maps of LDSX-6B after SHT trials (a) 1618 K (1345 °C)/20 h, (b) 1618 K (1345 °C)/40 h, and (c) 1633 K (1360 °C)/20 h.

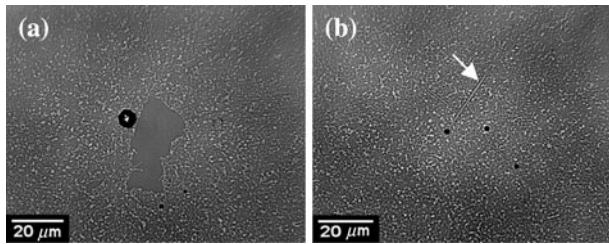


Fig. 12—Microstructures of LDSX-6C after SHT at 1588 K (1315 °C)/40 h (a) remnant interdendritic and (b) needle-like structures.

shifts to higher temperatures (approaching  $T_{BM}$  of the fully homogenized condition) during ramp. The SHT peak temperature should then be chosen as near as possible to the melting point of the alloy to promote solute diffusion and achieve compositional homogeneity in the material, taking into consideration the temperature spread that may be expected within the large industrial furnace to avoid incipient melting in the material that will lead to material scrap.

The typical SHT cycle in industry for single-crystal nickel-base turbine blades usually starts with a relatively fast ramp, followed by a progressive stepwise reduction

in the ramp rate when nearing the SHT peak temperature; this is to prevent temperature overshoots especially in a large industrial furnace. Dwell steps may be incorporated during the stepwise reduction in the ramp rate, usually after every ramp step to allow the furnace space to achieve better thermal equilibrium prior to the start of the next slower ramp step. The dwell also allows further diffusion to occur, but as the costs scale with time rather than temperature, the aim of the ramp optimization process is thus to raise the temperature as fast as possible consistent with the increase in  $T_{IM}$  on one hand and slow enough to ensure thermal stability throughout the furnace on the other. To ensure melting does not occur, commercial SHT cycles in current use adopt ramp profiles that are much more gentle than necessary to raise  $T_{IM}$ , resulting in time being wasted at too low a temperature, which equates to unnecessary cost. Clearly, a more useful approach would be to determine the  $T_{IM}$  quantitatively as the SHT progresses and to increase the temperatures used in the ramp profile accordingly to closely track the evolving  $T_{IM}$  to speed up the homogenization process.

The use of the DSC both to simulate the ramp, or critically part thereof, and then to investigate the effect

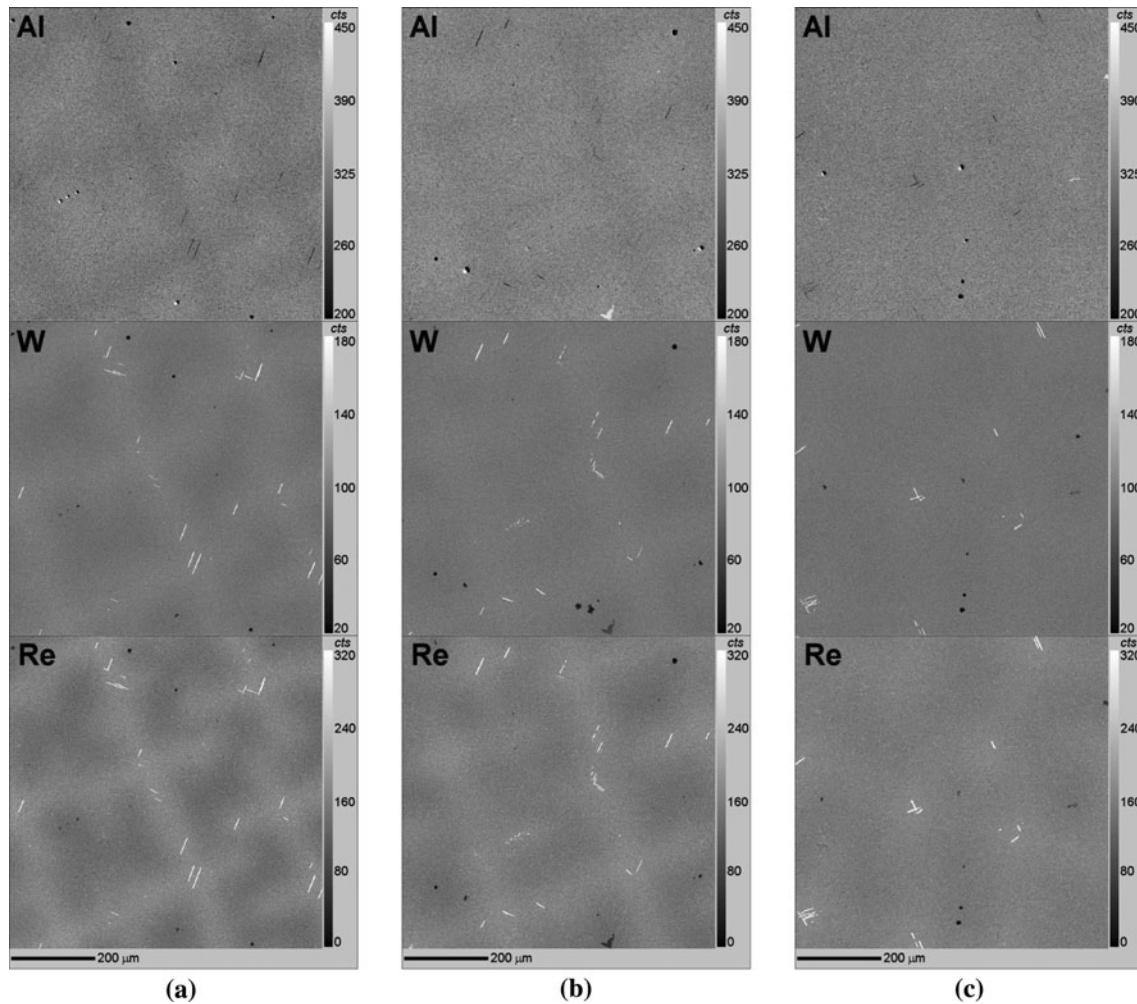


Fig. 13—EPMA maps of LDSX-6C after SHT trials: (a) 1593 K (1320 °C)/20 h, (b) 1593 K (1320 °C)/40 h, and (c) 1593 K (1320 °C)/80 h.

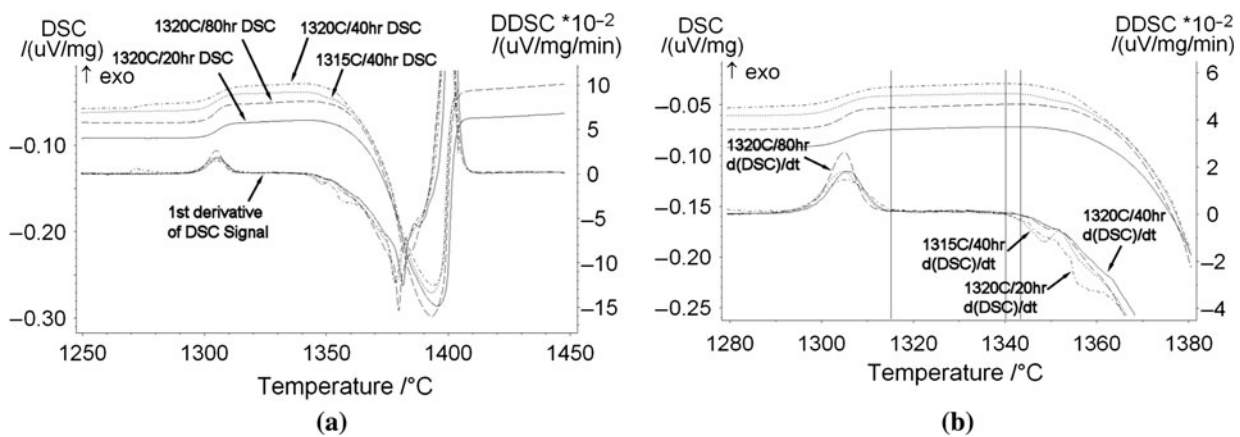


Fig. 14—DSC results of LDSX-6C after SHT trials (a), and (b) in higher detail.

of that particular part of the SHT ramp on a very small scale allows a ramp profile to be devised without the very high costs of full-scale trials. The current study has demonstrated that the DSC could accurately predict the outcome of the SHT trials in larger furnaces and has

sufficient sensitivity to detect, for example, the presence of remnant interdendritic at levels consistent with the current practice of inspection via optical microscopy. For example, the very slight amount of remnant interdendritic shown in LDSX-6C after the 1608 K

**Table X. Thermal Characteristics of LDSX-6C After SHT Trials**

	$\gamma'$ Solvus Start [K (°C)]	$\gamma'$ Solvus End [K (°C)]	$T_{IM}$ [K (°C)]	$T_{BM}$ [K (°C)]
1588 K (1315 °C)/40 h	1562 (1289)	1589 (1316)	1613 (1340)	1616 (1343)
1593 K (1320 °C)/20 h	1563 (1290)	1588 (1315)	1613 (1340)	1616 (1343)
1593 K (1320 °C)/40 h	1563 (1290)	1588 (1315)	—	1616 (1343)
1593 K (1320 °C)/80 h	1563 (1290)	1588 (1315)	—	1616 (1343)

(1335 °C) ramp was readily detected on the DSC trace. The DSC measurement has also provided a sufficiently accurate measure of the  $T_{IM}$  to avoid incipient melting.

The laboratory-scale vacuum furnace used in the current study also allows a much greater accuracy in the temperature control, where temperature variation in the hot zone was within  $\pm 1$  °C compared to the temperature variation in an industrial vacuum furnace that is typically up to  $\pm 5$  °C.<sup>[10,11]</sup> In addition, the hot zone of the laboratory-scale vacuum furnace is also significantly smaller compared to that of an industrial vacuum furnace, and as such, thermal equilibrium and uniformity in the former is expected to be achieved much more readily. The laboratory-scale vacuum furnace therefore allows the response of the alloys to any given SHT to be accurately quantified, which is particularly useful to quantify, for example, the response of the alloy to SHT in the cold spots or hot spots in an industrial vacuum furnace.

During the initial attempts to identify potential ramp profiles, the bulk melting temperatures  $T_{BM}$  of the alloys in as-cast condition were used to provide a first approximation of the maximum SHT peak temperature which could be used. The rationale behind this was that the  $T_{BM}$  is the temperature at which the alloy would melt if all the interdendritic areas could be eliminated after undergoing the ramp. Note that the  $T_{BM}$  of the alloy after ramp or full SHT is usually slightly higher compared to the as-cast  $T_{BM}$  of the alloy; therefore, estimating the maximum SHT peak temperature that could be used from the latter should give a greater degree of safety margins with regard to incipient melting. The maximum SHT peak temperature chosen for the alloys may be much lower compared to the  $T_{BM}$  of the alloy, sometimes by as much as 15 °C to 20 °C, to take into account various aspects of the SHT, which includes the safety margins required to avoid incipient melting, the temperature variability expected within an industrial furnace, and also sometimes depending on the availability of the SHT cycle in industry. If a particular alloy could be satisfactorily solution heat treated to achieve the required levels of compositional homogeneity with an established SHT cycle currently in use in industry, then this would allow time and cost savings with regard to queue time, temperature validation, and other related processes required to establish a new SHT cycle in industry.

With the various points set forth in mind, for both LDSX-6B and LDSX-6C of which the  $T_{BM}$  in as-cast condition were 1634 K and 1621 K (1361 °C and 1348 °C), respectively, ramp profiles with peak temperatures of 1618 K and 1608 K (1345 °C and 1335 °C) were chosen for the respective alloys during the initial attempt to identify potential ramp profiles. Note that

the peak temperatures of the chosen ramp profiles were higher than the  $T_{IM}$  of 1613 K and 1588 K (1340 °C and 1315 °C) for as-cast LDSX-6B and LDSX-6C, respectively; these should not pose a problem if all the interdendritic areas could be eliminated after the ramp and the melting only occurs at  $T_{BM}$  of the alloy. In the case of LDSX-6B, the interdendritic peak was completely removed and the  $T_{BM}$  is raised to 1637 K (1364 °C) after the 1618 K (1345 °C) ramp. In addition, incipient melting was not observed after extending the 1618 K (1345 °C) ramp to 1621 K (1348 °C), allowing the 1618 K (1345 °C) ramp to be used for LDSX-6B. For LDSX-6C, however, the results of the ramp profile evaluation and incipient melting check indicate the 1608 K (1335 °C) ramp was not suitable for this alloy as the ramp was unable to promote significant homogenization to raise the melting point of the alloy to near  $T_{BM}$  during the ramp, leading to localized incipient melting in this alloy during the ramp. Although it seems that the approach of approximating the maximum SHT peak temperature from as-cast  $T_{BM}$  works in the case of LDSX-6B, the failure of the 1608 K (1335 °C) ramp to promote homogenization and avoid incipient melting in LDSX-6C highlights the inadequacy of this approach; *i.e.*, it is not always correct to assume that the maximum SHT peak temperature could be approximated from the as-cast  $T_{BM}$ . The results of the SHT ramp profile evaluation and incipient melting check of both alloys with various ramp profiles highlight the fact that the suitability of the ramp profile does not depend on the SHT peak temperature alone; clearly, other important aspects to consider are the characteristics of the alloy to be solution heat-treated, the as-cast  $T_{IM}$ , and the duration of the dwells at critical temperatures necessary to promote homogenization and raise  $T_{IM}$ .

To compare the difference between the two alloys and the various ramp profiles and full SHT cycles, the details of the thermal characteristics of the alloys and the various parameters of the ramp profiles and full SHT cycles are summarized in Table XI. The intermediate dwell temperature  $T_{3\text{hours}}$  denotes the temperatures at which the 3-hour dwell were employed prior to reaching the SHT peak temperature in all the ramp profiles investigated in this study. Note also that the heat-treated  $\gamma'$  solvus start temperatures (Tables IX and X) were used in the comparison rather than the corresponding temperatures in the as-cast condition; the  $\gamma'$  solvus temperature has been mentioned to shift with the homogenization of the material, and the former is thought to be more representative of the temperature at which the  $\gamma'$  precipitates in the homogenized material would start to dissolve and the diffusional processes are sufficiently rapid to promote homogenization.



Table XI. Thermal Characteristics of Alloys; Various Parameters of the Ramp Profiles and Full SHT Cycles

Alloy	Heat-Treated $\gamma'$ Solvus Start [K (°C)]	As-Cast $T_{IM}$ [K (°C)]	As-Cast $T_{BM}$ [K (°C)]	Ramp Profile/SHT Cycle	$T_{3\text{hours}}$ [K (°C)]	SHT Peak $T$ [K (°C)]	Time in Ramp $T_{\gamma'}$ start - $T_{IM}$ (min)	Time in Ramp $T_{IM} - T_{\text{peak}}$ (min)
LDSX-6B	1581 (1308)	1613 (1340)	1634 (1361)	1618 K (1345 °C) 1633 K (1360 °C)/20 h	1608 (1335) 1623 (1350)	1618 (1345) 1633 (1360)	338 152	30 270
LDSX-6C	1563 (1290)	1588 (1315)	1621 (1348)	1588 K (1315 °C)/20 h 1593K (1320 °C) 1608 K (1335 °C)	1583 (1310) 1588 (1315) 1598 (1325)	1588 (1315) 1593 (1320) 1608 (1335)	420 362 142	0 60 280

On inspection of Table XI, it became apparent that the approach of using the as-cast  $T_{BM}$  alone to estimate the maximum SHT peak temperature was flawed; obviously, the as-cast  $T_{IM}$  also needs to be considered. For LDSX-6B, the chosen 1618 K (1345 °C) ramp includes a 3-hour intermediate dwell step at 1608 K (1335 °C), which was above the 1581 K (1308 °C)  $\gamma'$  solvus and below 1613 K (1340 °C) as-cast  $T_{IM}$ , promoting rapid homogenization without a significant risk of incipient melting. In contrast, the 1608 K (1335 °C) ramp chosen for LDSX-6C has the 3-hour intermediate dwell step at 1598 K (1325 °C), which was much higher than both the  $\gamma'$  solvus and the as-cast  $T_{IM}$ . As such, there was insufficient time at lower temperatures below the as-cast  $T_{IM}$  in the 1608 K (1335 °C) ramp to allow significant homogenization to occur prior to the temperature being raised above the  $T_{IM}$  as the ramp progresses, resulting in localized incipient melting.

In the attempt to devise a new ramp profile for LDSX-6C, the 1593 K (1320 °C) ramp profile was therefore devised by considering the as-cast  $T_{IM}$  of 1588 K (1315 °C) rather than the as-cast  $T_{BM}$ . The  $T_{3\text{hours}}$  was chosen to be 1588 K (1315 °C), which is equivalent to the as-cast  $T_{IM}$ ; therefore, the expectation was that the local  $T_{IM}$  could be raised above this temperature during the ramp prior to reaching the 3-hour intermediate dwell step to avoid the occurrence of incipient melting during this intermediate dwell step. During the incipient melting check, incipient melting was not observed in the 1592 K (1319 °C) sample, but minor occurrence of incipient melting was observed in the 1597 K (1324 °C) sample. The  $T_{IM}$  after the 3-hour intermediate dwell step at 1588 K (1315 °C) was therefore greater than 1592 K (1319 °C) and just under 1597 K (1324 °C). The choice of the  $T_{3\text{hours}}$  of 1588 K (1315 °C) was also limited by other factors; ideally, a lower temperature, *e.g.*, 1578 K to 1583 K (1305 °C to 1310 °C), should be chosen to improve the safety margins with regard to incipient melting, but it was noted that the  $\gamma'$  solvus end temperature after the 1608 K (1335 °C) ramp was 1593 K (1320 °C). As such, choosing an intermediate dwell step temperature that is too low would result in poor homogenization even though incipient melting may be avoided. This was indeed shown to be the case in the 1588 K (1315 °C)/40 hours full SHT cycle, where after a 3-hour intermediate dwell step at 1583 K (1310 °C) and a 40 hours soak at 1588 K (1315 °C), remnant interdendritic areas were still observed. The SHT peak temperature of 1593 K (1320 °C) could also be determined from the results of the incipient melting check. Further DSC ramp run to evaluate the suitability of the 1593 K (1320 °C) ramp profile was therefore deemed unnecessary as the temperature of the intermediate dwell step and the SHT peak temperature could be appropriately determined from prior data and the incipient melting check runs.

From Table XI, the response of the two alloys to ramp/full SHT could also be shown by comparing several SHT ramp profiles/SHT cycles that seem to have similar temperature margins and times spent in the various temperature regimes; these are (1) 1618 K (1345 °C) ramp

on LDSX-6B and 1593 K (1320 °C) ramp on LDSX-6C, and (2) 1633 K (1360 °C) SHT cycle on LDSX-6B and 1608 K (1335 °C) ramp on LDSX-6C. For the 1618 K (1345 °C) ramp on LDSX-6B and the 1593 K (1320 °C) ramp on LDSX-6C, prior to reaching as-cast  $T_{IM}$ , the time spent in the high temperature regime between the  $\gamma'$  solvus start and as-cast  $T_{IM}$  were nearly similar at approximately 6 hours. However, the response of the two alloys to these ramps was vastly different. For LDSX-6B after the 1618 K (1345 °C) ramp, neither the incipient melting nor the remnant interdendritic areas were observed; the interdendritic peak on the DSC trace was completely removed, and the  $T_{BM}$  was raised to 1637 K (1364 °C). However, for LDSX-6C after the 1593 K (1320 °C) ramp, although incipient melting was not observed, a significant amount of remnant interdendritic areas were still observed (Figures 9(a) and (b)); therefore, the  $T_{IM}$  was not expected to have shifted significantly. Even after the full 1593 K (1320 °C)/20 hours SHT, a small amount of remnant interdendritic areas was still observed although the  $T_{IM}$  was raised to approximately 1613 K (1340 °C). The difference in the responses of the two alloys highlights the less segregated nature of as-cast LDSX-6B, which is therefore easier to homogenize compared to as-cast LDSX-6C.

Similarly, on examining the 1633 K (1360 °C) full SHT on LDSX-6B and the 1608 K (1335 °C) ramp on LDSX-6C, the intermediate 3-hour dwell step temperature was almost 10 °C above the as-cast  $T_{IM}$ , and the time spent between  $\gamma'$  solvus start up to as-cast  $T_{IM}$  was approximately 2.5 hours in both cases. After the 1608 K (1335 °C) ramp, significant incipient melting was observed in LDSX-6C but the LDSX-6B alloy that has been heat-treated with the 1633 K (1360 °C)/20 hours full SHT did not show any incipient melting. This result again shows that although the time for homogenization up to as-cast  $T_{IM}$  was relatively similar, the absence of incipient melting in LDSX-6B after the 1633 K (1360 °C)/20 hours full SHT again highlights the less segregated state of as-cast LDSX-6B, resulting in more rapid dissolution of interdendritic areas and an increase in  $T_{IM}$  with time during the ramp such that incipient melting is avoided compared to LDSX-6C.

Moving on to the effects of the SHT peak temperature and soak period, better homogeneity was achieved with higher SHT peak temperatures and/or longer soak periods. These observations are expected as higher SHT peak temperatures and/or longer soak periods promote the diffusional processes required for the homogenization process. The LDSX-6B SHT trials comparing the effectiveness of the SHT peak temperature and soak period demonstrated that doubling the soak period from 20 hours to 40 hours was more effective in homogenizing the alloy than increasing the SHT peak temperature by 15 °C from 1618 K to 1633 K (1345 °C to 1360 °C).

For the LDSX-6C alloy, the SHT peak temperature seems to have a strong effect on the homogeneity achieved after SHT. Good homogeneity was noted after SHT at 1593 K (1320 °C)/40 hours. However, when the SHT peak temperature was lowered by 5 °C and SHT was carried out at 1588 K (1315 °C)/40 hours, significant amount of remnant interdendritic areas was

observed in the material. It was noted that the  $\gamma'$  solvus end temperature after the 1588 K (1315 °C)/40 hours SHT was approximately 1589 K (1316 °C); therefore, not all  $\gamma'$  would have been dissolved during this SHT even though homogenization is still occurring albeit at a slower pace, resulting in the significant remnant interdendritic areas observed after this SHT. Although it seems that the homogeneity of LDSX-6C is highly sensitive to the lower SHT peak temperature of 1588 K (1315 °C) compared to 1593 K (1320 °C), such is the case because the SHT peak temperature has to be chosen to be very low as a consequence of this alloy being more highly segregated in the as-cast condition; as such, this alloy has higher susceptibility to incipient melting, limiting the SHT window. To avoid incipient melting in this alloy, the higher temperatures in the SHT window could not be used, which limits the homogeneity that could be achieved after SHT. Note that the  $\gamma'$  solvus end temperature of LDSX-6C is 1588 K (1315 °C) even after prolonged soak at 1593 K (1320 °C) for 80 hours (Table X); as such, the effectiveness of the SHT at 1588 K (1315 °C)/40 hours is poor as one would expect. The temperature of 1588 K (1315 °C) that is the  $\gamma'$  solvus end defines the lower bound, and 1597 K (1324 °C), where some minor incipient melting occurred, defines the upper bound.

## B. Alloy Effects

The DSC traces of the alloys in as-cast condition show the phase transformations associated with  $\gamma'$  dissolution, melting of interdendritic areas, and bulk melting of the material. The gentle exothermic deviation in the as-cast condition could be confirmed to be associated with  $\gamma'$  dissolution as evident from the transformation of the gentle deviation into a sharper and more distinct bump after ramp or full SHT. In as-cast condition, the gentle deviation implies that  $\gamma'$  dissolution occurs over a range of temperatures, whereas the sharper and more distinct bump after ramp or full SHT meant that the  $\gamma'$  dissolution is more abrupt and occurs at a more distinct temperature. In the as-cast condition, the  $\gamma$  dendrites, and therefore the  $\gamma'$  precipitates that were precipitated in solid state on cooling, are expected to have a spread in composition due to preferential elemental partitioning to the solid or liquid during solidification. After the ramp or full SHT, the composition of the  $\gamma'$  precipitates becomes much more distinct as a consequence of the homogenization that occurs, resulting in the more distinct  $\gamma'$  dissolution on the DSC trace.

The as-cast DSC results also show that the end of the  $\gamma'$  dissolution seems to commensurate with the as-cast  $T_{IM}$ , which is start of the interdendritic peak. Similar DSC results have been reported by other researchers on single-crystal nickel-base superalloy.<sup>[12]</sup> The likely explanation is that due to solute partitioning during solidification and the large freezing range, some local areas in the  $\gamma$  dendrites may have  $\gamma'$  solvus temperatures that are much higher or equivalent to the temperature at which the last interdendritic areas solidify; therefore, the end of the  $\gamma'$  dissolution seems to commensurate with the as-cast  $T_{IM}$ . After ramp or full SHT,  $\gamma'$  dissolution

occurs much more distinctly at lower temperatures compared to  $T_{IM}$  due to homogenization of the highly segregated  $\gamma$  dendrite areas.

The first small peak observed on the DSC trace could be categorically associated with melting of the interdendritic areas, where the magnitude of the minor peak was typically found to be correlated to the amount of remnant interdendritic areas observed in the microstructure. The decreasing magnitude of the minor peak after ramp correlates to the decreasing remnant interdendritic areas in the microstructure, whereas after full SHT, the absence of the interdendritic peak in the DSC trace typically corresponds to the absence of remnant interdendritic areas in the microstructure.

The position and the relative proportions of the interdendritic peak and bulk melting peak on the as-cast DSC trace can be used as a measure of the proportion of the interdendritic and dendrite areas in the microstructure and/or the level of compositional segregation between the interdendritic and dendrite areas in the as-cast condition. The closely spaced peaks of as-cast LDSX-6B show that the dendritic and interdendritic areas solidify at a relatively similar range of temperatures and, therefore, may be more similar in composition compared to as-cast LDSX-6C. These observations are consistent with the EPMA results that show the greater elemental segregation in as-cast LDSX-6C. The interdendritic peak is also of a smaller proportion of the bulk melting peak for as-cast LDSX-6B compared to as-cast LDSX-6C, showing that less energy is required to melt the interdendritic areas of as-cast LDSX-6B, which may be an indication of lower fraction of interdendritic areas and/or less segregated nature of the interdendritic areas in this alloy. After ramp/full SHT, the reduction in the area under the interdendritic peak, which may be accompanied by a shift of the interdendritic peak toward the bulk melting peak on the DSC traces indicate the degree of dissolution of the interdendritic areas as well as the reduction of elemental segregation between the dendrite and interdendritic areas.

Comparing the two alloys, as-cast LDSX-6B is less segregated and has a larger “apparent” SHT window (approximately 95 K (95 °C) from the  $\gamma/\gamma'$  solvus start temperature to  $T_{IM}$  in the as-cast condition), whereas as-cast LDSX-6C shows a higher degree of segregation and a smaller corresponding “apparent” SHT window of approximately 65 K (65 °C). Strictly speaking, the SHT window should be taken from the  $\gamma/\gamma'$  solvus end temperature up to  $T_{IM}$ , but in the as-cast condition, this would not be meaningful as the  $\gamma/\gamma'$  solvus end temperature usually coincides with the  $T_{IM}$ . Nevertheless, as a result, LDSX-6B is comparatively easier to homogenize and is less susceptible to incipient melting. The interdendritic areas of LDSX-6B dissolve more readily after being subjected to the ramp, and solution heat-treated samples of LDSX-6B have good compositional homogeneity and remnant interdendritic areas were no longer observed. The larger SHT window of LDSX-6B, which after the 1618 K (1345 °C) ramp was approximately 19 K (19 °C), also meant that this alloy is more able to tolerate deviations in the SHT process in industry without compromising the final compositional homogeneity

achieved. This is in comparison to LDSX-6C, where remnant interdendritic areas were still observed after the ramp and this alloy was also highly susceptible to incipient melting. The SHT window of LDSX-6C is less than 10 °C ( $\gamma/\gamma'$  solvus end temperature of 1588 K [1315 °C] even after prolonged 1593 K [1320 °C]/80 hours SHT and incipient melting observed at 1597 K [1324 °C] after the 1593 K [1320 °C] ramp). Therefore, for the LDSX-6C alloy, the process window is smaller, and tighter control has to be put in place that may incur additional costs to ensure the final material is neither undersolutioned nor has sustained incipient melting.

The compositions of the two alloys are relatively similar; however, they show very different responses to SHT. In the as-cast condition, it is clear that the degree of segregation of the elements Ta, W, and Re in LDSX-6C is much greater than in LDSX-6B, even though the two alloys have identical contents with respect to these elements. Cr, and to a greater extent Mo, has been shown to have a strong beneficial effect in reducing the degree to which W and Re partition to the dendrite core during solidification.<sup>[13]</sup> It seems therefore that even with the high Cr content of 6.5 wt pct, the lack of Mo in LDSX-6C has caused greater segregation of W and Re to the  $\gamma$  dendrite compared to LDSX-6B, which has a lower Cr content of 2.5 wt pct but with 1.0 wt pct Mo present. The EPMA maps of as-cast LDSX-6B do indeed show marginally greater levels of W and Re in the interdendritic areas compared to as-cast LDSX-6C in Figure 4.

The significantly higher Cr and Hf contents of LDSX-6C have also caused greater segregation of these two elements in this alloy. In LDSX-6C, Cr has a unique segregation pattern with a fairly even distribution in the  $\gamma$  dendrites and a generally lower concentration in the interdendritic areas, but the highest concentration was found in the final material to solidify at the edges of the interdendritic region. Similarly, the highest concentrations of Hf are also found in those areas with the highest Cr concentrations in LDSX-6C. The interdendritic region has been shown to have two distinct morphologies, *i.e.*, (1) the fine  $\gamma/\gamma'$  morphology and (2) the coarse cellular  $\gamma'/\text{wide } \gamma$  channel structure.<sup>[14]</sup> Immediately after the end of primary solidification ( $L \rightarrow \gamma$ ), solidification of the interdendritic region commences in areas that show the fine  $\gamma/\gamma'$  morphology; this is followed by a gradual transition to the formation of the coarse cellular  $\gamma'/\text{wide } \gamma$  channel structure that continues until the terminal stages of solidification.<sup>[14]</sup> Therefore, the  $T_{IM}$  inferred from the DSC trace for the alloys in as-cast condition is the temperature at which melting of the coarse cellular  $\gamma'/\text{wide } \gamma$  channel structure commences. It is precisely in the coarse cellular  $\gamma'$  areas that the maximum Cr and Hf concentrations are found in LDSX-6C, and the susceptibility of this alloy to incipient melting therefore seems to be linked to these areas with greater Cr and Hf concentrations. During solidification, Cr partitions to the solid with a modest partition coefficient of 1.04 to 1.11 depending on the alloy,<sup>[13]</sup> which is similar to other elements such as Co and Mo. In contrast, W and Re segregate strongly to the solid, with partition coefficients of 1.32 to 1.63 for Re and 1.19 to 1.31 for W, depending on the alloy.<sup>[13]</sup> Due



to the high Cr content in LDSX-6C and both W and Re being more strongly segregated to the solid, a high concentration of Cr is left in the liquid after primary solidification. Rejection of Cr from the  $\gamma'$  phase during solidification of the interdendritic region and the high volume fraction of  $\gamma'$  phase in the interdendritic areas contribute to large amounts of Cr being rejected, leading to very high concentrations of Cr in the remnant liquid and therefore in the coarse cellular  $\gamma'$  interdendritic areas formed in the final stages of solidification. The partition coefficient of Hf in nickel-base superalloys is not well documented. However, based on the concentrations of Hf observed in the EPMA map, this element seems to be mildly segregating to the liquid, and the higher Hf content of LDSX-6C again causes a buildup of this element in the remnant liquid at the terminal stages of solidification and therefore the high concentrations of Hf at the edge of the interdendritic areas. Even at the lower Cr and Hf levels of LDSX-6B, the concentration of Cr is higher in the  $\gamma$  dendrites and lower in the interdendritic regions, but again there is also a slight build-up of Cr and Hf concentrations at the edge of the interdendritic areas (Figure 4(a)), although not as marked as in LDSX-6C.

Although the higher elemental segregation in LDSX-6C could in part be attributed to the lack of Mo to reduce the segregation of W and Re to the  $\gamma$  dendrites, by far the greater culprit is the high Cr content, which was not compensated by a decrease in the contents of W and Re. In LDSX-6C, stronger partitioning of W and Re to the  $\gamma$  dendrites due to a lack of Mo and the high Cr content causes large amounts of Cr to be rejected to the liquid after the saturation of Cr in the  $\gamma$  dendrites during primary solidification. This was followed by a marked absence of Cr in the interdendritic areas that form immediately after as Cr is strongly rejected from the  $\gamma'$  phase, and the large amounts of Cr left in the liquid lead to the formation of areas with very high concentrations of Cr at the terminal stages of solidification, which was even greater than the concentration of Cr in the  $\gamma$  dendrites. This represents a large variation in the solute gradient of Cr going from the dendrite core to the interdendritic areas up to the last areas to solidify in LDSX-6C as shown in Figure 4(b). The corresponding solute variation of Cr in LDSX-6B was less drastic due to the lower Cr content in this alloy. These factors lead to the higher segregation in LDSX-6C.

In addition, LDSX-6C also shows the presence of TCP precipitates after the full SHT cycles. Although further work has yet to be carried out to investigate these precipitates, their needle-like morphology which is typical of TCP phases, as well as the high W and Re contents of these precipitates as shown in the EPMA maps confirm these precipitates to be TCP phases. The DSC is unlikely to be able to detect the phase transformation associated with TCP phase formation as the volume fraction of the TCP phases formed seems extremely low ( $<1$  pct). The TCP precipitates were formed during SHT, likely to be due to the supersaturation of TCP-forming elements in the dendrite cores of the alloy in as-cast condition, which was not sufficiently reduced during the SHT ramp. The greater segregation of W and Re in the

$\gamma$  dendrites due to the absence of Mo and the high Cr concentration in the  $\gamma$  dendrite is expected to increase the propensity of TCP phase formation significantly in LDSX-6C.<sup>[13]</sup> This may also be confounded by the lower Ru content of 3 wt pct in this alloy compared to LDSX-6B, as such TCP phase precipitation could not be completely suppressed in LDSX-6C. A Ru content of up to 5 wt pct has previously been shown to be effective in suppressing the precipitation of TCP phases in Re-containing nickel-base superalloys.<sup>[15]</sup> To minimize the formation of TCP precipitates during SHT, the supersaturation of TCP-forming elements in the dendrite cores would need to be reduced by incorporating additional dwell steps at lower temperatures into the ramp profile. Because TTT diagrams for TCP phase formation were usually characterized for the homogenized material, they would not be applicable in the current situation where the TCP phases form due to the highly segregated dendrite core in the as-cast condition. Additional work would be required to characterize the TTT curves for the highly segregated as-cast dendrite core, and from these TTT curves, the choice of temperature and hold time for the additional dwell steps could be chosen appropriately to the left of the TTT curve, balancing the temperature required to promote diffusion and reduce the strong segregation of TCP-forming elements in the dendrite cores against the appearance of TCP phases within the hold time at these temperatures.

The current study also highlights the need to balance alloy compositions to cater for the various requirements in service with the ability to process these materials. The additions of W and Re are known to be beneficial to the mechanical properties, whereas better environmental protection properties could be attained with higher Cr and lower Mo. However, excessive Cr addition increases the TCP phase formation propensity in these alloys. In terms of processing, it was found that Cr, and to a greater extent Mo, have strong beneficial effects on the castability of alloys. However, as shown in the current study the addition of excessive Cr without adjusting other alloying additions may result in an alloy that is more highly segregated and difficult to solution heat-treat.

## VI. SUMMARY AND CONCLUSIONS

This study presents an iterative SHT optimization process that has the potential to continuously raise the robustness and effectiveness of the SHT cycle to give improved homogenization. Two alloys of relatively similar compositions but showing significantly different responses to SHT are compared.

A summary of the work carried out and the conclusions that can be drawn from the current study is as follows:

1. A methodological approach has been used to optimize the SHT of two fourth-generation single-crystal nickel-base superalloys LDSX-6B and LDSX-6C as follows:

- (a) Evaluate as-cast material properties
  - (b) Identify potential SHT ramp profiles
  - (c) Assess suitability of the SHT ramp profile
  - (d) Identify safety margins available with regard to incipient melting
  - (e) Assess effect of SHT peak temperature and soak period
2. DSC measurements and EPMA mapping were carried out to investigate the material properties in the as-cast condition and after SHT. The DSC apparatus was also adopted as a vacuum furnace to evaluate the suitability of the SHT ramp profile and to check the safety margins with regard to incipient melting.
  3. LDSX-6B in as-cast condition was found to have lower degree of elemental microsegregation; hence, this alloy homogenizes relatively easily in the SHT trials. Good homogeneity was achieved in LDSX-6B for all three SHT trials carried out at 1618 K (1345 °C)/20 hours, 1618 K (1345 °C)/40 hours, and 1633 K (1360 °C)/20 hours.
  4. LDSX-6C in the as-cast condition was found to have a higher degree of elemental microsegregation. Hence, this alloy is much more difficult to homogenize and is also highly prone to incipient melting. Good homogeneity was achieved in LDSX-6C with both the 1593 K (1320 °C)/40 hours and 1593 K (1320 °C)/80 hours cycles.
  5. After SHT, both alloys retained some residual microsegregation, and the LDSX-6C alloy showed TCP phase precipitation at dendrite cores.
  6. Increases in SHT peak temperature and/or soak period resulted in improved compositional homogeneity in the materials as expected. The appropriate SHT process may be determined based on the required homogeneity.

#### ACKNOWLEDGMENTS

The authors would like to acknowledge the support of Professor A.L. Greer at the Department of

Materials Science and Metallurgy for the provision of facilities and Rolls-Royce plc. through the Rolls-Royce UTP at the University of Cambridge for the provision of materials and funding. The authors also wish to express appreciation to Dr. Chris Hayward at the School of Geosciences, University of Edinburgh (previously at the Department of Earth Sciences, University of Cambridge) for carrying out the EPMA mapping work in this study and to Mr. Kevin Roberts of the Department of Materials Science and Metallurgy for assistance in carrying out the solution heat treatment trials.

#### REFERENCES

1. G.L. Erickson: *JOM*, 1995, vol. 47, pp. 36–39.
2. G.E. Fuchs and B.A. Boutwell: *Mater. Sci. Eng. A*, 2002, vol. 333A, pp. 72–79.
3. M.S.A. Karunaratne, P. Carter, and R.C. Reed: *Mater. Sci. Eng. A*, 2000, vol. A281, pp. 229–33.
4. G.E. Fuchs: *Mater. Sci. Eng. A*, 2001, vol. 300A, pp. 52–60.
5. B.C. Wilson, J.A. Hickman, and G.E. Fuchs: *JOM*, 2003, pp. 35–40.
6. R.A. Hobbs, G.J. Brewster, C.M.F. Rae, and S. Tin: *Superalloys 2008*, TMS, Warrendale, PA, 2008, pp. 171–80.
7. S.J.B. Reed and A. Buckley: *Virtual WDS. Mikrochim. Acta Suppl.*, 1996, vol. 13, pp. 479–83.
8. W.J. Boettinger and U.R. Kattner: *Metall. Mater. Trans. A*, 2002, vol. 33A, pp. 1779–94.
9. N. D'Souza and H.B. Dong: *Superalloys 2008*, TMS, Warrendale, PA, 2008, pp. 261–70.
10. N. Jones and I.M. Edmonds: Private communications, Sept 2010.
11. T-M Vacuum Products Inc.: Pacer Series Vacuum Furnace Product Sheet 05-10 & Performer Series Vacuum Furnace Product Sheet 02-06, T-M Vacuum Products Inc., Cinnaminson, NJ.
12. L.A. Chapman: *J. Mater. Sci.*, 2004, vol. 39, pp. 7229–36.
13. R.A. Hobbs, S. Tin, and C.M.F. Rae: *Metall. Mater. Trans. A*, 2005, vol. 36A, pp. 2761–73.
14. H.T. Pang, H.B. Dong, R. Beanland, H.J. Stone, C.M.F. Rae, P.A. Midgley, G. Brewster, and N. D'Souza: *Metall. Mater. Trans. A*, 2009, vol. 40A, pp. 1660–69.
15. R.A. Jones: MPhil. Dissertation, University of Cambridge, Cambridge, U.K., 2008.